Characterization of Calcium Phosphate Spherical Particles in the Subretinal Pigment Epithelium—Basal Lamina Space in Aged Human Eyes

Matthew G. Pilgrim, PhD,[1,2,3] Salma Marouf, MD,[4] Sarah Fearn, PhD,[5] Lajos Csincsik, PhD,[3]
Elod Kortvely, PhD,[6] Jonathan C. Knowles, PhD,[2] Goldis Malek, PhD,[7] Richard B. Thompson, PhD,[8]
Imre Lengyel, PhD[3]

Purpose: Micrometer-sized spherules formed of hydroxyapatite or whitlockite were identified within extracellular deposits that accumulate in the space between the basal lamina (BL) of retinal pigment epithelium (RPE) and the inner collagenous layer of Bruch's membrane (sub-RPE—BL space). This investigation aimed to characterize the morphologic features, structure, and distribution of these spherules in aged human eyes with and without clinical indications of age-related macular degeneration (AMD).

Design: Experimental study.

Participants: Five human eyes with varying degrees of sub-RPE—BL deposits were obtained from the University College London Institute of Ophthalmology and Moorfield's Eye Hospital Tissue Repository or the Advancing Sight Network. Two eyes were reported as having clinical indications of AMD (age, 76—87 years), whereas 3 were considered healthy (age, 69—91 years).

Methods: Cadaveric eyes with sub-RPE—BL deposits were embedded in paraffin wax and sectioned to a thickness of 4-10 μm. Spherules were identified and characterized using high-resolution scanning electron microscopy (SEM), energy-dispersive x-ray spectroscopy, and time-of-flight secondary ion mass spectroscopy.

Main Outcome Measures: High-resolution scanning electron micrographs of spherules, the size-frequency distribution of spherules including average diameter, and the distribution of particles across the central-peripheral axis. Elemental maps and time-of-flight secondary ion mass spectra also were obtained.

Results: The precipitation of spherules is ubiquitous across the central, mid-peripheral, and far-peripheral axis in aged human eyes. No significant difference was found in the frequency of spherules along this axis. However, statistical analysis indicated that spherules exhibited significantly different sizes in these regions. In-depth analysis revealed that spherules in the sub-RPE—BL space of eyes with clinical signs of AMD were significantly larger (median diameter, 1.64 μm) than those in healthy aged eyes (median diameter, 1.16 μm). Finally, spherules showed great variation in surface topography and internal structure.

Conclusions: The precipitation of spherules in the sub-RPE—BL space is ubiquitous across the central—peripheral axis in aged human eyes. However, a marked difference exists in the size and frequency of spherules in eyes with clinical signs of AMD compared to those without, suggesting that the size and frequency of spherules may be associated with AMD. *Ophthalmology Science 2021;1:100053 © 2021 by the American Academy of Ophthalmology. This is an open access article under the CC BY-NC-ND license (http://creativecommons.org/licenses/by-nc-nd/4.0/).*

📖 Supplemental material available at www.ophthalmologyscience.org.

The accumulation of extracellular deposits in the space between the basal lamina (BL) of the retinal pigment epithelium (RPE) and the inner collagenous layer of the Bruch's membrane (BrM) is a universal feature in the aged human eye.[1–6] This space, referred to as the sub-RPE—BL space, is the location of drusen and basal linear deposits.[6,7] Herein, these 2 types of deposit are described collectively as sub-RPE—BL deposits, which are distinct from basal laminar deposits that accumulate between the basal lamina and plasma membrane of RPE cells.[6,7]

Sub-RPE—BL deposits can be present minimally in healthy aged eyes without a predisposition to disease.[8] Conversely, sub-RPE—BL deposits also have been associated with age-related disorders, some of which result in irreversible loss of vision.[2,5,9,10] For example, sub-RPE—BL deposits are considered the earliest pathologic hallmark of age-related

macular degeneration (AMD).[1,11] How sub-RPE−BL deposits contribute to disease pathogenesis and vision loss is not yet understood fully; however, it is thought that the extracellular deposits in the sub-RPE−BL space block essential metabolic exchange between photoreceptor cells and the underlying choroidal vasculature, eventually leading to irreversible damage and loss of vision.[12,13]

The accumulation of mineral constituents within the sub-RPE−BL space was first described more than half a century ago, with the authors of the study describing "bits of calcium" within large drusen.[14,15] In addition, a subsequent study that used von Kossa staining described "black staining particles" and "large nodular aggregates of calcium" within sub-RPE−BL deposits.[16] This was despite elemental or mineral analyses, or both, not having been performed. Later studies confirmed the enrichment of calcium within sub-RPE−BL deposits using energy-dispersive x-ray spectroscopy and synchrotron micro-focus x-ray fluorescence.[17,18] Elemental analysis performed in combination with electron microscopy established that calcium and phosphorus enrichment was associated with small spherical particles that were 0.5 to 5.0 μm in diameter.[17] More recently, the combination of mineral phase analysis and confocal fluorescence microscopy led to the identification of small (0.5−20 μm in diameter), hollow, spherical particles that were formed of hydroxyapatite.[13] In addition, a second study that used electron diffraction mineral analysis reported that some of these spherules were formed of whitlockite, a magnesium-substituted tricalcium phosphate.[19]

Experiments that combined immunohistochemical labelling of spherical particles with hydroxyapatite fluorescent staining demonstrated the localization of proteins characteristic of drusen to the surface of hydroxyapatite spherules.[13] Proteins were able to bind to the surface of spherules either as a single protein or in combination with others.[13] Accordingly, a novel mechanism for drusen biogenesis and growth was hypothesized.[13] This comprised 4 stages: (1) the accumulation of lipid droplets in the sub-RPE−BL space, (2) the precipitation of hydroxyapatite on the surface of lipid droplets resulting in hydroxyapatite-encrusted lipid particles, (3) the binding of proteins to hydroxyapatite spherules, and (4) the oligomerization, cross-linking, or both of proteins to hydroxyapatite-bound proteins leading to sub-RPE−BL deposit growth.[13]

To understand further how spherules contribute to the pathogenesis of ocular diseases, this investigation aimed to gain a significantly better understanding of the morphologic features, structure, and distribution of calcified spherical particles that were recently identified as an ubiquitous constituent of sub-RPE−BL deposits.[13] In this study, a high-resolution multimodal approach that included scanning electron microscopy (SEM), energy-dispersive x-ray spectroscopy (EDX), and time of flight-secondary ion mass spectrometry (TOF-SIMs) was used.

Methods

Sample Source

Before these experiments, ethics committee approval was obtained (identifier, 10/H0106/57-2014ETR44). All research adhered to the tenets of the Declaration of Helsinki. The requirement for informed consent was waived because of the retrospective nature of the study. Five human cadaveric eyes (age, 69−91 years; see Table 1 for details) with varying degrees of sub-RPE−BL deposits were obtained from the University College London Institute of Ophthalmology and Moorfield's Eye Hospital Tissue Repository or the Advancing Sight Network (previously Alabama Eye Bank). Of these eyes, 1 was diagnosed clinically with AMD and 1 exhibited clinically identifiable soft drusen. The 3 additional eyes were considered normal aged human eyes.

Cadaveric eyes were enucleated 3 to 24 hours after death and fixed in 1% glutaraldehyde with 4% paraformaldehyde. After the removal of the anterior segment, fixed tissues were embedded in paraffin wax using a Leica ASP300S tissue processor. Using an RM2225 microtome, multiple consecutive paraffin-embedded cross-sections with a thickness of 4 to 10 μm were generated.

For experimental analysis, consecutive sections from each eye were examined. A single slide was used for high-resolution SEM and elemental analyses. A second slide was examined using SEM to determine the frequency and distribution of spherules across the central−peripheral axis. Finally, a third consecutive section was interrogated using time-of-flight secondary ion mass spectrometry.

Table 1. Gender, Age, Eye, and Ocular Pathological Features of 5 Aged Human Eyes Containing Sub−Retinal Pigment Epithelium Deposits

Eye No.	Gender	Age (yrs)	Eye	Ocular Pathological Findings
1 (AMD87)	Female	87	Unknown	• AMD (dry) • Hyperlipidemia • Osteoarthritis
2 (2390_16)	Unknown	76	Left	• Soft drusen present • Ciliochoroidal melanoma
3 (2315)	Unknown	79	Unknown	• Squamous cell carcinoma
4 (2071_98A)	Female	91	Left	• Retina seems normal, but with focal regions of outer retinal degeneration • Some retinal pigment epithelial migration
5 (687_99)	Male	69	Left	• Choroidal melanoma

AMD = age-related macular degeneration.
Note that eyes 1 and 2 had clinically identifiable drusen or AMD pathologic features.

Scanning Electron Microscopy of Human Cadaveric Eyes

Scanning electron microscopy (SEM) enabled the generation of high-resolution images of spherical particles, including surface topography and internal structure. Paraffin wax was removed from tissues using xylene treatment followed by washing with ethanol (xylene, xylene, xylene, 1:1 xylene and 100% ethanol, 100% ethanol, 100% ethanol). Dewaxed tissues then underwent chemical critical point drying using hexamethyldisilazane. Fixed and dehydrated tissues on glass slides were mounted on aluminum stubs (Agar Scientific) using conductive adhesive tabs (Agar Scientific). To ensure conductivity of the sample surfaces, double-sided copper tape with a conductive acrylic adhesive was used to form a conductive bridge from the underside of the stub to the surface of the glass slide (Ted Pella, Inc). Samples were then sputter-coated with 1 nm of platinum or carbon (Cressington Scientific Instruments UK).

Scanning electron microscopy was performed using a Zeiss Sigma VP Field emission SEM (Carl Zeiss AG) or a Philips XL30 field emission gun SEM (FEI). Electron micrographs were obtained at low and high magnifications and using both in-lens and back-scattered electron detectors. High-resolution electron micrographs were obtained using the in-lens detector, an accelerating voltage of 3 kV, an aperture size of 30 μM, and a working distance of 2 to 4 μm. Backscattered electron micrographs were obtained using the backscattered electron detector, an accelerating voltage of 10 to 20 kV, an aperture of 120 μm, and a working distance of 8 to 10 μm.

Density-Dependent Color Scanning Electron Microscopy

Density-dependent color SEM enabled the simultaneous visualization of surface structure and compositional difference within a single high-resolution image. Density-dependent color SEM electron micrographs were generated using the image processing programme ImageJ as follows: a secondary electron micrograph and a backscattered electron micrograph of the same region were opened in ImageJ using the RGB Grey Merge plugin. The secondary electron image was assigned the green channel, and the back-scattered electron micrograph was set to the red channel. Regions containing elements with relatively large atomic numbers (z), like mineral deposits, would exhibit orange or red hues, whereas regions comprising elements with relatively low z numbers, like those that form organic tissues, would be visible as green hues.

Energy Dispersive X-Ray Spectroscopy

Energy-dispersive x-ray spectroscopy was used to confirm the elemental composition of spherical particles. Energy-dispersive x-ray spectroscopy was performed using a Philips XL30 field emission gun SEM (FEI) equipped with an Oxford Instruments energy-dispersive x-ray spectroscopy elemental analysis system (Oxford Instruments). An accelerating voltage of 20 kV, an aperture of 5 units, and a working distance of 10 mm was used. Gold and palladium sputter coating was avoided because of x-ray emission energies characteristic of gold overlapping with the KL3 peak of phosphorus. Elements of interest included calcium, phosphorus, and magnesium.

Time-of-Flight Secondary Ion Mass Spectrometry Analysis of Spherical Particles

Time-of-flight secondary ion mass spectrometry is a materials science technique that is capable of identifying molecular fragment ions characteristic of inorganic calcium phosphates. This methodology was used to confirm that the spherical particles observed on scanning electron micrographs were also composed of an inorganic calcium phosphate, likely hydroxyapatite.[13,20]

Time-of-flight secondary ion mass spectrometry was performed using an ION-TOF ToF.SIMS5 (ION-TOF) equipped with a bismuth primary ion beam (Bi_3^+) operating at 25 kV. A Bi_3^+ cluster was used for the analyses because it generates a high secondary ion yield in tissue samples. For charge compensation, the time-of-flight secondary ion mass spectrometry was equipped with a low-energy electron flood gun. Before mass spectrometry, contaminants on the sample surface were removed by bombarding the upper surface of the sample with a 10-KeV Ar_n^+ cluster ion beam (10 KeV Ar_{1000}^+). Subsequently, the Bi_3^+ primary ion beam was used to sputter secondary ions from the sample surface. Sputtered ions were directed into a time-of-flight mass analyzer and the molecular weight of each secondary ion determined by the time it took for the ion to reach the mass analyzer. Mass spectrometry was performed over the range of 0 to 880 m/z.

Analyzing Size-Frequency and Distribution of Spherical Particles across the Central-Peripheral Axis

The use of ultra-widefield imaging methods for ophthalmic examinations successfully highlighted an association between peripheral sub-RPE—BL deposits and diseases such as AMD.[2,21] Accordingly, high-resolution SEM was used to determine whether the size and number of spherules or the distribution of spherical particles across the central—peripheral axis contribute to AMD pathogenesis. Human eyes with and without clinical indications of AMD were examined.

Samples were prepared as described for SEM. Using low-magnification SEM, the center of the retina was identified. Electron micrographs were obtained from the center of the retina to the ora serrata at the far periphery. Each image showed approximately 600 μm of the RPE—BrM complex along this axis. The BrM was oriented as close to horizontal as possible with the apical side of the BrM pointing toward the top of the image (Supplemental Fig 1). To ensure that the entirety of the central—far peripheral axis was imaged, images were overlapped by 50% (Supplemental Fig 1: arrow, arrowhead, and asterisk highlight anatomic markers). Based on the number of images and the level of image overlap, the length of the central—far peripheral axis could be approximated (Supplemental Table 1). The axis then was divided into 3 equal regions that were assigned the central region, mid periphery, and far periphery.

Next, high-magnification images of the RPE—BrM complex were collected along the entire length of the central—far peripheral axis. The number of spherules within each image was recorded, and the total number of spherules within each of the 3 regions was calculated. The diameter of individual spherules was determined via image analysis using ImageJ. The scale of each image was calibrated using the straight line and set scale functions. The area of the image covered by each spherical particle was then obtained using the oval function of ImageJ and converted into diameter (in micrometers) using the equation: diameter = $(\sqrt{area / \pi}) \times 2$.

Statistical Analysis

Statistical analyses were performed using SPSS statistics software (IBM) or GraphPad Prism (GraphPad Software, Inc). To investigate whether a significant difference was present in the total number of spherules in the central region, mid periphery, and far periphery, 1-way analysis of variance was used. In addition, 2-way analysis of variance was used to identify significant differences in the mean diameter of spherules in the central region, mid
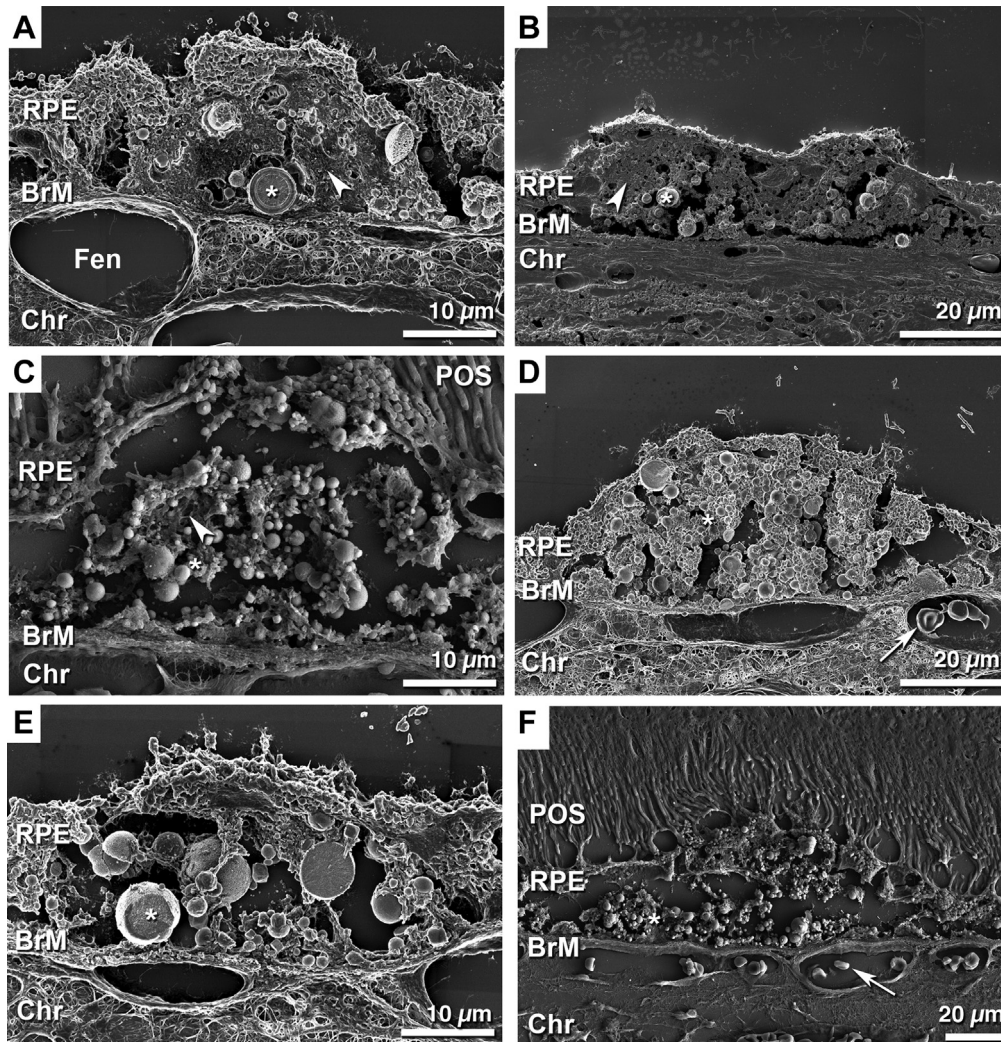
Figure 1. A—F, Scanning electron micrographs showing deposits in the space between the basal lamina of the retinal pigment epithelium (RPE) and the inner collagenous layer of Bruch's membrane (sub-RPE—BL) in aged human eyes. All examined sub-RPE—BL deposits contained spherical particles as well as showing variation in size, shape, and ultrastructure. **A, C, E,** Focal drusen exhibiting morphologic features consistent with small, hard drusen. **B, D, F,** Deposits in the sub-RPE-BL that were reminiscent of larger soft drusen or basal linear deposits. Scale bars: (**A**) 10 μm, (**B**) 20 μm, (**C**) 10 μm, (**D**) 20 μm, (**E**) 10 μm, (**F**) 20 μm. Asterisk indicates spherical particle, arrowhead indicates extracellular material, and arrows indicates red blood cell. BrM = Bruch's membrane; Chr = choroid; Fen = fenestrae; POS = photoreceptor outer segment.

periphery, and far periphery. Mann—Whitney U test statistical analysis was used to compare the average size of spherical particles in eyes with clinical indications of AMD versus normal aged eyes (non-AMD eyes).

Results

Scanning Electron Microscopy of Deposits in the Space between the Basal Lamina of the Retinal Pigment Epithelium and the Inner Collagenous Layer of Bruch's Membrane in Aged Human Eyes

In all eyes examined in this study, numerous sub-RPE—BL deposits were visible between the basal lamina of the RPE and the inner collagenous layer of BrM (Fig 1). A considerable variation in the size and shape of deposits was observed within and between eyes (Fig 1). Importantly, spherules were present in all sub-RPE—BL deposits, with some spherules surrounded by extracellular organic material (Fig 1A, arrowhead). In addition, individual spherical particles without any surrounding material were observed between the basal lamina of the RPE and the basally located BrM (Fig 2).

Scanning Electron Microscopy Revealed Spherical Particle Surface Topography and Internal Structure Heterogeneity

Spherical particles displayed heterogeneity in surface topography (Fig 3). Based on the observed surface structure, spherules were designated smooth (Fig 3A), rough (Fig 3B),
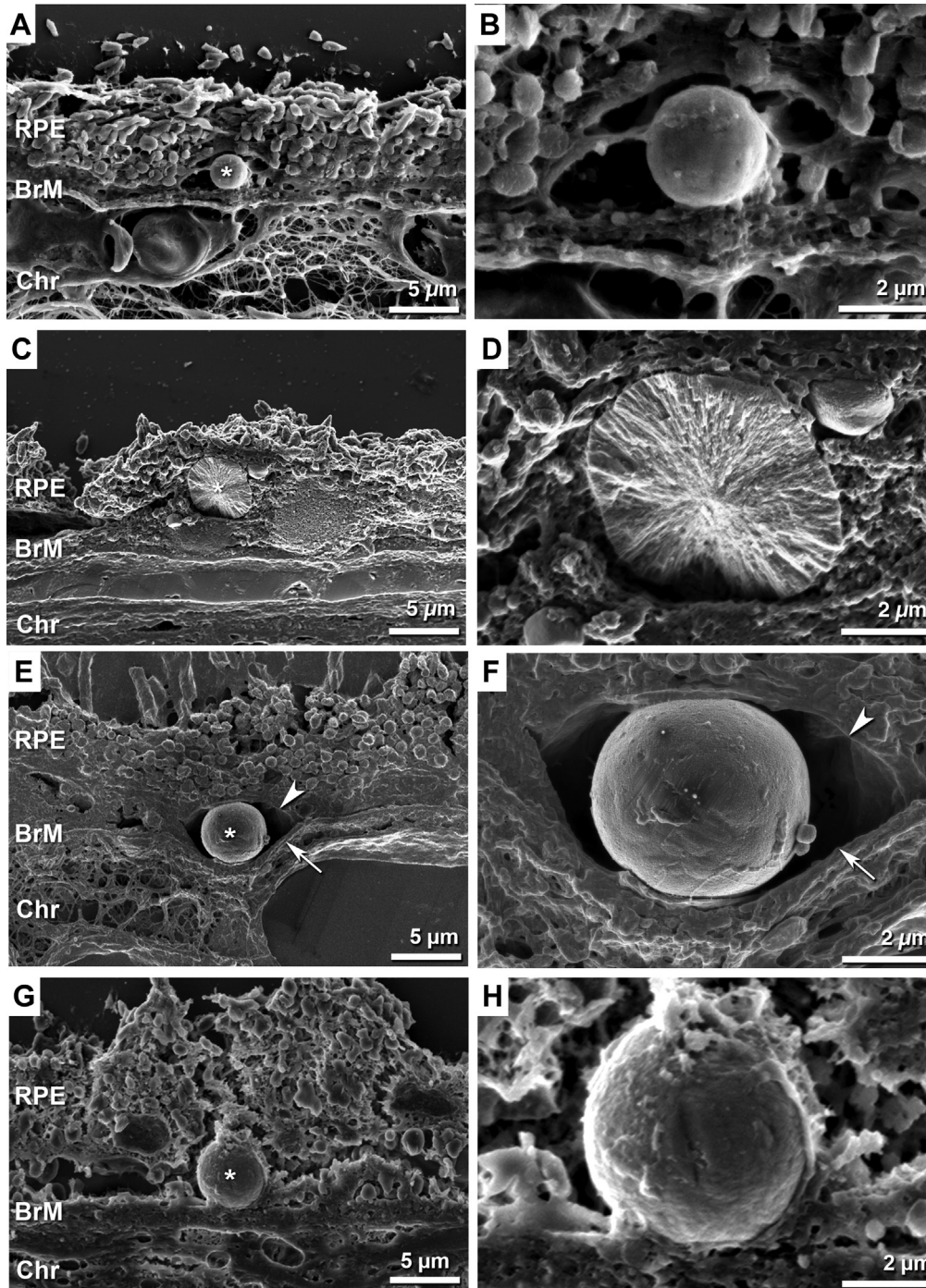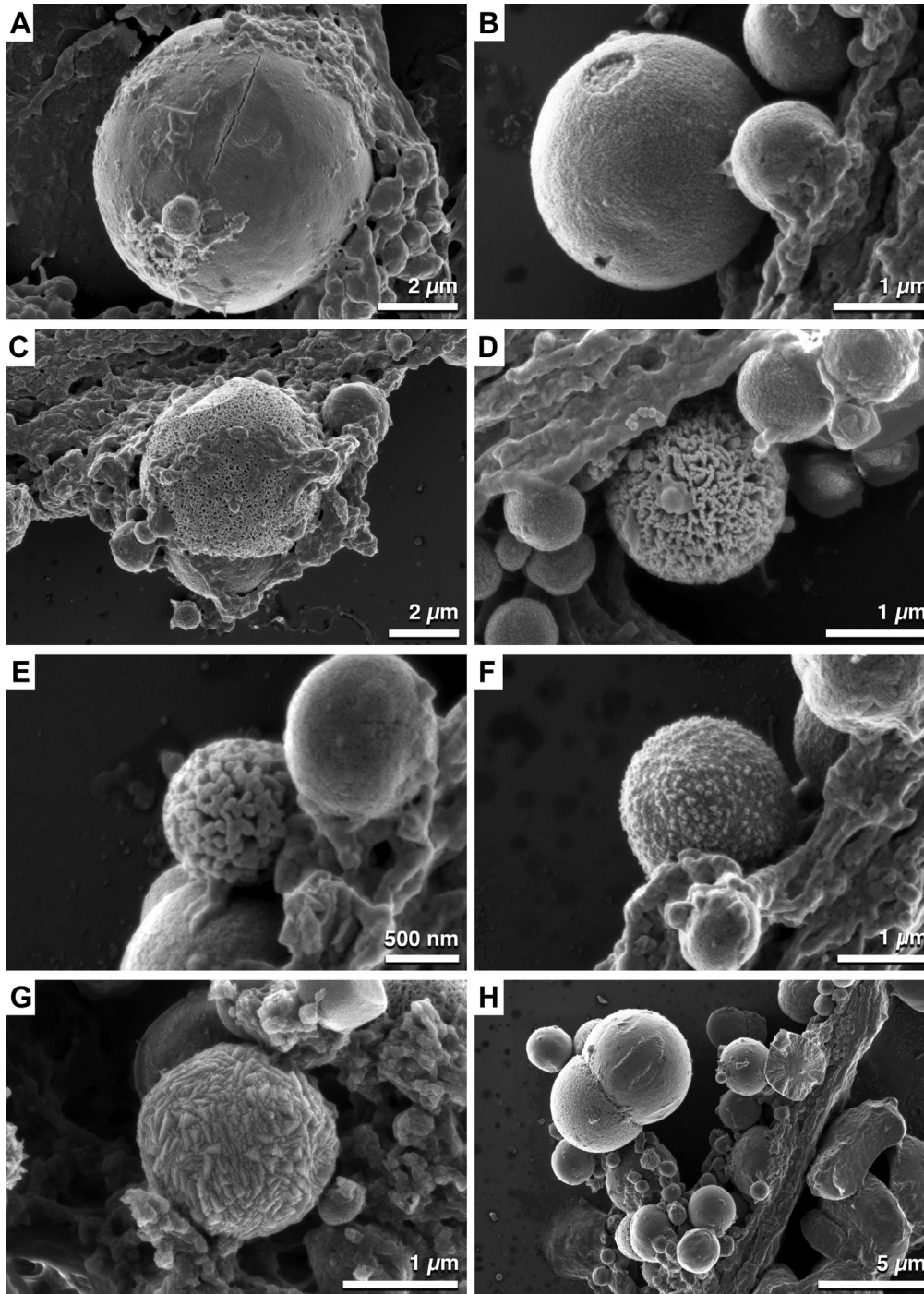
Figure 2. **A–H**, Scanning electron micrographs showing isolated spherules occurring between the basal lamina of the retinal pigment epithelium (RPE) and the inner collagenous layer of the Bruch's membrane (BrM). **A, C, E, G**, Low-magnification scanning electron micrographs showing isolated spherules. **B, D, F, H**, High-magnification scanning electron micrographs showing isolated spherules. Scale bars: (**A, C, E, G**) 5 μm, (**B, D, F, H**) 2 μm. Asterisk indicates spherical particle, white arrowhead indicates basal lamina of RPE, and white arrow indicates inner collagenous layer of Bruch's membrane. Chr = choroid.

sponge-like (Fig 3C, D), globular (Fig 3E, F), geometric (Fig 3G), or lobed (Fig 3H). Remarkably, the surface topography of the lobed spherules also exhibited surface structure variation.

The internal structure of spherules also showed variation (Fig 4). In this study, at least 5 distinct internal structures were observed. These included spherules containing crystal-like structures that orientated from the center of the

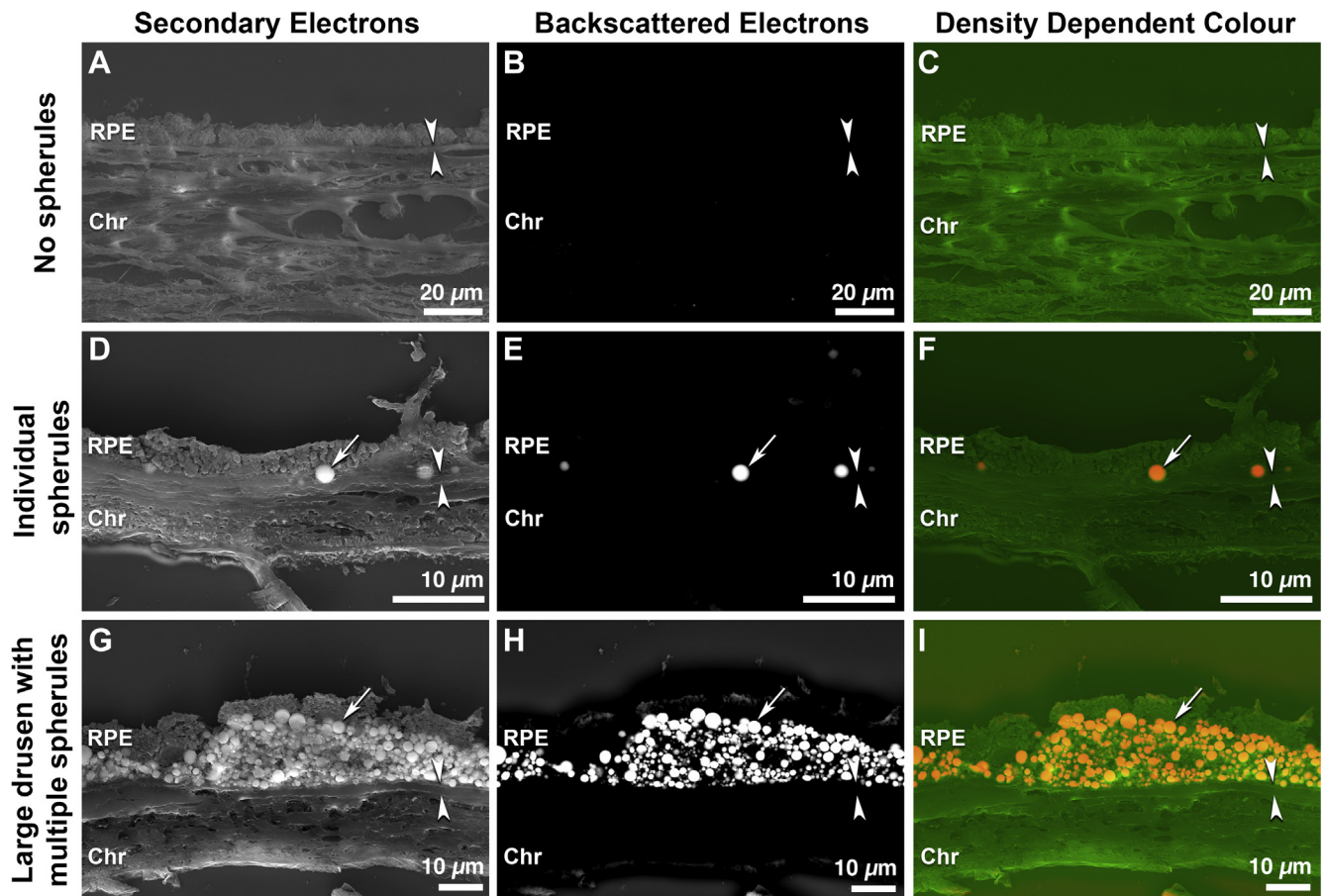**Figure 3.** **A–H**, Scanning electron micrographs showing spherical particles within deposits in the space between the basal lamina of the retinal pigment epithelium and the inner collagenous layer of Bruch's membrane exhibiting surface heterogeneity. High-resolution scanning electron microscopy identified surface structure heterogeneity of spherules. Based on the surface topography, spherules were described as (**A**) smooth, (**B**) rough, (**C, D**) sponge-like, (**E, F**) globular, (**G**) geometric, and (**H**) lobed. Scale bar: (**A**) 2 μm, (**B**) 1 μm, (**C**) 2 μm, (**D**) 1 μm, (**E**) 500 nm, (**F**) 1 μm, (**G**) 1 μm, and (**H**) 5 μm.

spherule to the surface (Fig 4A–C), spherical particles with apparent concentric growth rings (Fig 4D), particles with a distinct core and shell (Fig 4E), spherules that exhibited crystal-like structures external to a distinct solid core (Fig 4F), and spherules that seemed to contain stalagmite and stalactite structures that protruded inward (Fig 4G).
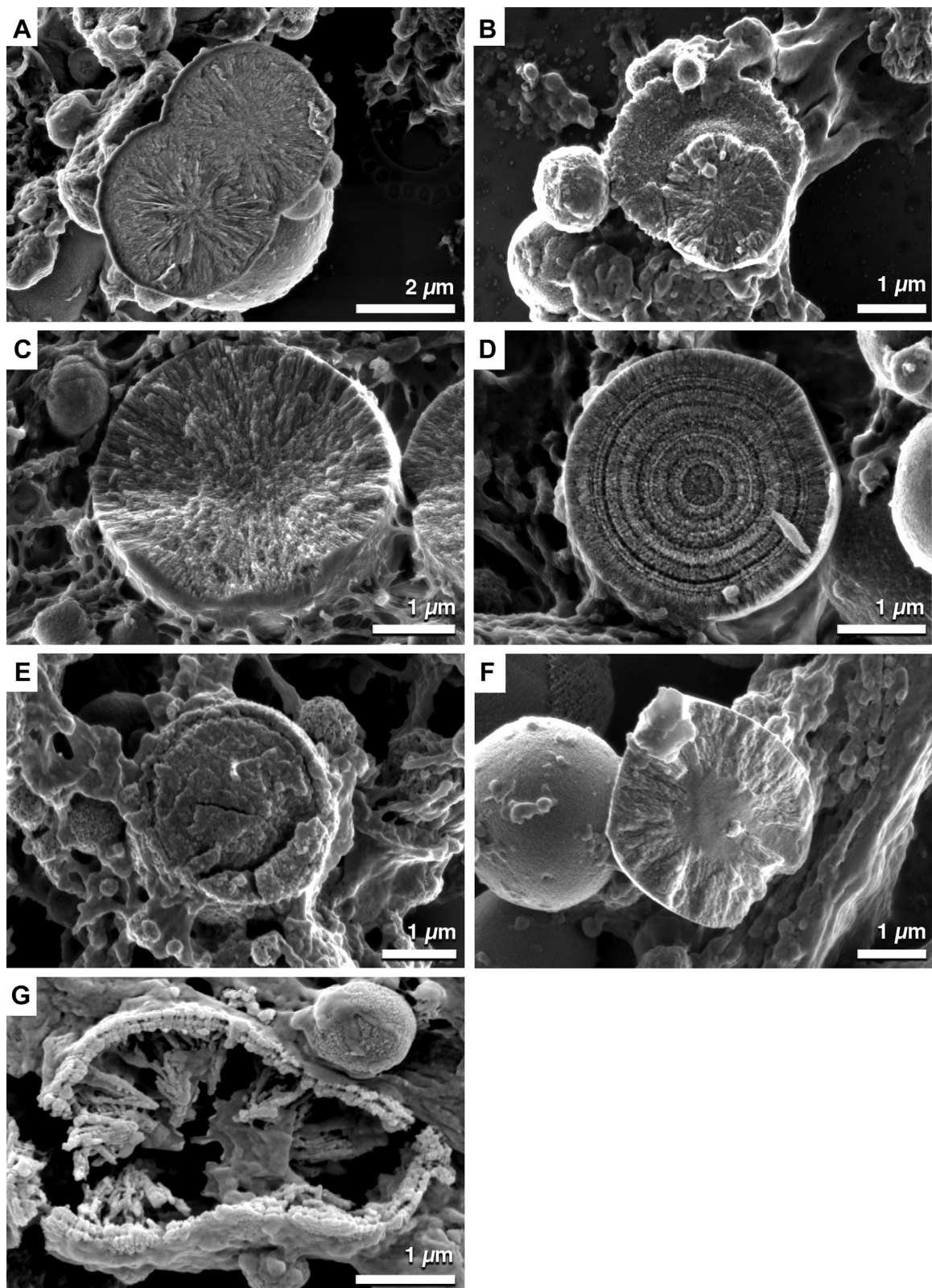
Figure 4. **A–G**, Scanning electron micrographs showing spherical particles displaying internal structure heterogeneity. **A–C**, Spherules contain crystal-like structures that extend outward from the spherule center. **D**, Spherical particles contain a series of concentric rings suggesting that spherules are formed by concentric mineral deposition. **E**, A distinct core and outer shell also are observed within spherical particles. **F**, A solid core surrounded by crystal or needle-like structures extending outward. **G**, Stalactite and stalagmite-like structures protruding inward from a distinct shell with an appearance similar to a bilayer. Scale bars: (**A**) 2 μm and (**B–G**) 1 μm.

Figure 5. A−I, Examination of deposits in the space between the basal lamina of the retinal pigment epithelium (RPE) and the inner collagenous layer of Bruch's membrane (sub-RPE−BL) with density-dependent color scanning electron microscopy. **A, D, G**, High-resolution secondary electron micrographs of the RPE−Bruch's membrane (BrM) complex in aged human eyes. **B, E, H**, Backscattered electron microscopy of the RPE−BrM complex in aged human eyes. The contrast between spherules (white) and organic tissues (black) suggests that spherules are composed of elements of higher atomic number compared with those elements that form organic tissues. **F, G, I**, Density-dependent color scanning electron micrographs provide a map of potential mineral deposits (red and orange) surrounded by soft biological tissues (green). **A−C**, Density-dependent color scanning electron micrographs obtained from a region without spherical particles within the sub-RPE−BL space. **D−F**, Individual spherules (orange hues), possibly those that nucleate sub-RPE−BL deposit formation, located in the sub-RPE−BL space. **G−I**. Large sub-RPE−BL deposit containing numerous spherical particles (orange and red hues) composed of higher z-number elements. Scale bars: (**A−C**) 20 μm and (**D−I**) 10 μm. Arrows indicate spherules, and arrowheads delimit Bruch's membrane. Chr = choroid.

Density-Dependent Color Scanning Electron Microscopy of Deposits in the Space between the Basal Lamina of the Retinal Pigment Epithelium and the Inner Collagenous Layer of Bruch's Membrane in Aged Human Eyes

To investigate the differences in density between spherules and organic tissue, density-dependent color SEM was used. In regions of aged eyes that exhibited a healthy retinal−choroid complex, spherical particles were not readily identifiable in the sub-RPE−BL space (Figs 5A−C). However, when spherules were present, either as individual spherules located between the basal lamina of the RPE and the inner collagenous layer of BrM (Fig 5D−F) or as components of large basal linear deposits (Fig 5G−I), density-dependent color SEM was able to successfully identify spherules in the sub-RPE−BL space.

Energy-Dispersive X-Ray Spectroscopy of Spherical Particles within Deposits in the Space between the Basal Lamina of the Retinal Pigment Epithelium and the Inner Collagenous Layer of Bruch's Membrane

Energy-dispersive x-ray spectroscopy confirmed that calcium, phosphorus, and magnesium were present within spherules. Discrete emission peaks at approximately 1.25 keV, 2.01 keV, 3.39 keV, and 4.01 keV, corresponding to magnesium KL3, phosphorus KL3, calcium KL3, and calcium KM2, respectively, were clearly present on x-ray emission spectra (Fig 6B) obtained from spherical particles (Fig 6A). Elemental mapping of calcium (Fig 6C) and phosphorus (Fig 6D) confirmed the enrichment of these elements within spherules. However, elemental mapping could not differentiate magnesium signatures originating from
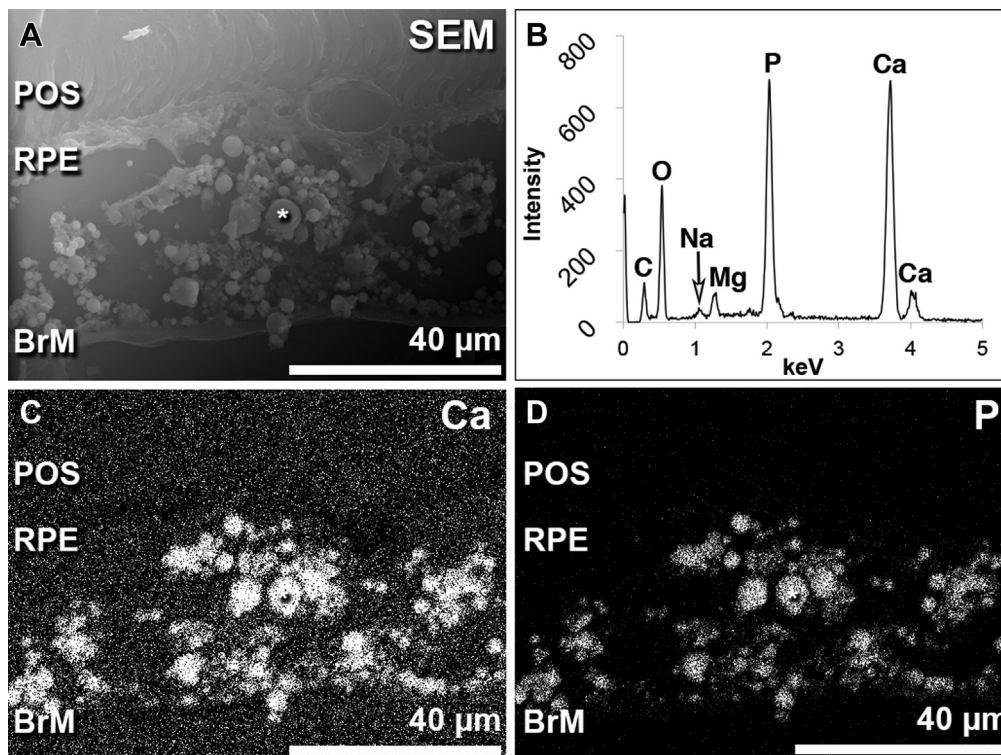
Figure 6. A—D, Elemental analysis of deposits in the space between the basal lamina of the retinal pigment epithelium (RPE) and the inner collagenous layer of Bruch's membrane (sub-RPE—BL) that contain spherical particles. **A,** Scanning electron micrograph showing a sub-RPE—BL deposit containing numerous spherical particles. The atrophied RPE monolayer is an indicator of advanced dry age-related macular degeneration. **B,** Graph showing a typical x-ray emission spectrum obtained from a single spherule. The large peaks present at emission wavelengths of approximately 2.01 keV, 3.39 keV, and 4.01 keV, corresponding to phosphorus (P) KL_3, calcium (Ca) KL_3, and Ca KM_2, respectively. Importantly, a small peak at approximately 1.25 keV corresponding to magnesium (Mg) KL_3 is also present. Peaks at 0.27 and 0.5 keV corresponding to carbon (C) and oxygen (O), indicating organic tissue, also were present. These elements can be attributed to both the spherule and surrounding tissues. Finally, a small peak at approximately 1.05 keV that corresponds to sodium (Na) is also present. This is likely to originate from the underlying glass slide as well as the sample tissue. **C,** Elemental map showing the distribution of calcium within sub-RPE—BL deposits. Calcium signal is enriched within spherules. **D,** Elemental map indicating that phosphorus also is enriched within spherical particles. BrM = Bruch's membrane; POS = photoreceptor outer segment.

spherical particles and the surrounding organic tissues. As is expected from organic tissues, emission energies of approximately 0.27 keV, 0.52 keV, and 1.04 keV corresponding to carbon (KL3), oxygen (KL3), and sodium (KL3) were readily detected. Of note, an emission peak at approximately 1.74 keV also was present. This peak is specific to silicon (KL3), which is expected to arise from the underlying glass substrate.

Time-of-Flight Secondary Ion Mass Spectrometry Analysis of Spherical Particles within Deposits in the Space between the Basal Lamina of the Retinal Pigment Epithelium and the Inner Collagenous Layer of Bruch's Membrane

The molecular composition of spherical particles also was analyzed using time-of-flight secondary ion mass spectrometry. Using this materials science technique, mass spectra and secondary ion maps were generated for molecular ions of

specific interest, including calcium phosphate minerals and proteins.

Secondary molecular ions associated with calcium phosphate minerals were detected readily on mass spectra (Fig 7A, A1, A2). Molecular ion peaks at 39.99 m/z, 47.01 m/z, 102.96 m/z, and 158.94 m/z corresponding to $[Ca^+]$, $[PO^+]$, $[CaPO_2^+]$, and $[Ca_2PO_3^+]$, respectively, were clearly visible (Fig 7A) (Ca, calcium; P, phosphorus; O, oxygen). Furthermore, numerous molecular ions separated by 55.9 m/z, which corresponds to a $[CaO^+]$ molecular ion and a building block of hydroxyapatite minerals, were also readily detected (Fig 7A, A1, A2; Table 2). Mapping the secondary fragment ions confirmed the localization of calcium phosphate molecular ions to spherical particles (Fig 7B, red). In addition to calcium phosphate fragment ions, molecular ions indicative of proteins also were detected within drusen (Fig 7B, green). These included amino acid fragments ions corresponding to glycine $[CH_4N^+]$, alanine $[C_2H_6N^+]$, proline $[C_4H_8N^+]$, valine $[C_4H_{10}N^+]$, leucine $[C_5H_{12}N^+]$, aspartic acid $[C_3H_6NO_2^+]$, glutamic acid $[C_4H_8NO_2^+]$, and histidine $[C_5H_8N_3^+]$ (C, carbon; H, hydrogen; N, nitrogen).
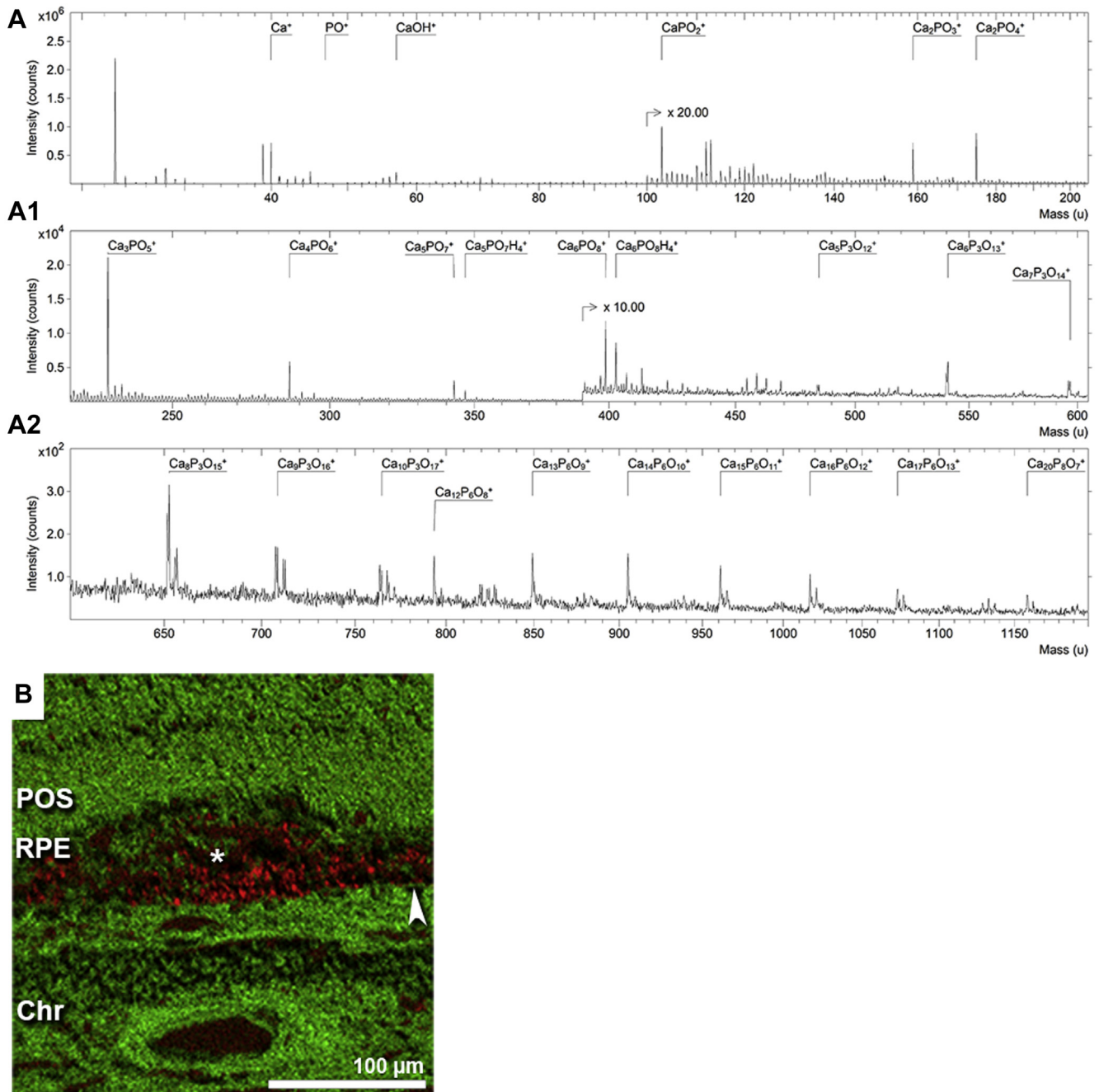
Figure 7. A, **B**, Time-of-flight secondary ion mass spectroscopy of deposits in the space between the basal lamina of the retinal pigment epithelium (RPE) and the inner collagenous layer of Bruch's membrane (sub-RPE—BL) containing numerous spherical particles. **A**, **A1**, **A2**, Single representative mass spectrum obtained from a sub-RPE—BL deposit containing numerous spherical particles. Secondary molecular ions corresponding to calcium, phosphate, and multiple calcium phosphate fragments ions were readily detectable within the region of interest. **B**, A secondary ion map showing that calcium phosphate fragment ions (red) localize to spherical particles, whereas the secondary molecular ions associated with proteins (green) are localized to organic matter and soft tissues. Scale bar: 100 μm. Asterisk indicates drusen, arrowhead indicates BrM. Ca = calcium; Chr = choroid; H = hydrogen; O = oxygen; P = phosphorus; POS = photoreceptor outer segment.

Size-Frequency Distribution of Spherical Particles in Aged Human Eyes

To determine the size-frequency distribution of spherules, a cumulative total of 12 667 spherules from all aged eyes were measured. The size frequency distribution of spherules was not normally distributed, and spherules exhibited diameters ranging from 0.12 to 12.53 μm in diameter. The mean diameter of all spherules was 1.74 μm, whereas the median diameter was 1.55 μm. The inter-quartile range for all spherules was 1.08 to 2.17 μm in diameter.

Table 2. Molecular Fragment Ions Indicative of Hydroxyapatite Identified by Time-of-Flight Secondary Ion Mass Spectroscopy

Fragment Ion	Mass (μm)
Ca^+	39.9889
PO^+	47.0074
$CaOH^+$	57.0018
$CaPO_2^+$	102.9572
$Ca_2PO_3^+$	158.9427
$Ca_2PO_4^+$	174.9539
$Ca_3PO_5^+$	230.8777
$Ca_4PO_6^+$	286.7986
$Ca_5PO_7^+$	342.887
$Ca_6PO_8^+$	398.8615
$Ca_5P_3O_{12}$	484.5304
$Ca_6P_3O_{13}$	540.6326
$Ca_7P_3O_{14}$	596.5688
$Ca_8P_3O_{15}$	652.4338
$Ca_9P_3O_{16}$	708.325
$Ca_{10}P_3O_{17}$	764.6632

Ca = calcium; H = hydrogen; O = oxygen; P = phosphorus.

Size-Frequency Distribution of Spherical Particles in Aged Human Eyes with and without Clinical Pathologic Features Indicative of Age-Related Macular Degeneration

The size frequency distribution of spherical particles in eyes with clinical indications of AMD (n = 2) were compared with those considered normal aged eyes (n = 3), and neither group showed a normal distribution (Fig 8). The median diameter of spherical particles in eyes with clinical indication of AMD was 1.64 μm, with an interquartile range of 1.18 to 2.26 μm (n = 9609 spherules). The
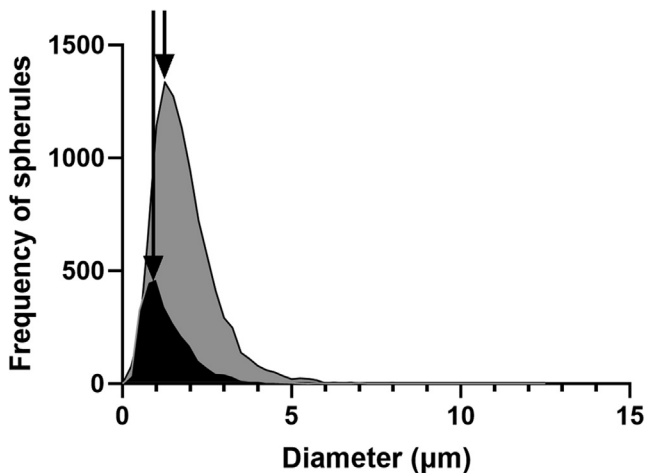
Figure 8. Graph showing the size frequency distribution of spherules in normal aged human eyes (n = 3) and eyes with clinical evidence of age-related macular degeneration (AMD; n = 2). Spherical particles from eyes with clinical indications of AMD eyes (grey) and non-AMD eyes (black) exhibited a nonnormal distribution. The frequency of spherules was markedly greater in eyes with clinical indications of AMD compared with normal aged eyes. Further, increased frequency of spherules with larger diameters was observed in eyes with AMD pathologic features compared with eyes without AMD. This is depicted by the shift in peak (arrows).

median diameter of spherules in normal aged eyes was 1.16 μm, with an interquartile range of 0.79 to 1.74 μm diameter (n = 2658 spherules). Statistical analysis (Mann−Whitney U test) indicated that the median diameter of spherules in eyes with clinical evidence of AMD was significantly different from those considered normal aged eyes (P = 0.001).

Size-Frequency Distribution of Spherical Particles in the Central Region, Mid Periphery, and Far Periphery of Aged Human Eyes

The size-frequency distribution of spherules within the central region, mid periphery, and far periphery of all aged eyes also was investigated. In the central region, spherical particles ranged from 0.12 to 11.91 μm (n = 3654 spherules; mean diameter, 1.96 μm; median diameter, 1.74 μm); in the mid periphery, spherules ranged from 0.24 to 12.52 μm (n = 5095 spherules; mean diameter, 1.84 μm; median diameter, 1.65 μm); whereas in the far periphery, spherules ranged from 0.12 to 8.92 μm (n = 3518 spherules; mean diameter, 1.35 μm; median diameter, 1.16 μm). Statistical analysis (2-way analysis of variance) indicated that the mean diameters of spherules in these 3 regions were not identical (P = 0.0001).

Analysis of Spherule Distribution across the Central Region, Mid Periphery, and Far Periphery in Aged Human Eyes

In the eyes examined in this study, 3654, 5095, and 3518 spherules were identified within the central region, mid periphery, and far periphery, respectively. One-way analysis of variance identified no significant difference in the total number of spherules in these 3 regions (F = 0.117; P = 0.891). Accordingly, the distribution of spherules across these 3 regions was examined in each of the eyes in this small cohort (Table 3). As shown in Table 3, great variation occurred between individual eyes. For example, 11% of spherules were localized to the central region of eye 1, whereas 52% of spherules were localized to the central region in eye 2. Further, 86% of all spherules were localized to the far periphery of eye 1, whereas only 10% of spherules were observed in the far periphery of eye 3 (Table 3).

Discussion

The high-resolution imaging approach used in this study provided new insights into the morphologic features, size, and distribution of calcified spherules that previously were hypothesized to be involved in sub-RPE−BL deposit biogenesis.[3,13,19] Herein, direct support that spherules contribute to this proposed mechanism of deposit formation is provided. Moreover, our in-depth analysis indicated that spherule size is narrowly restricted and that the distribution of spherules across the central−peripheral axis varies greatly amongst aged human eyes. Importantly, this study also found that spherical particles that accumulate

Table 3. Comparison of the Number of Spherules Present in the Central, Mid-Peripheral, and Far-Peripheral Regions in All Examined Eyes (n = 5)

Region	No. of Spherules							
	Eye 1	Eye 2	Eye 3	Eye 4	Eye 5	Total	Mean	Standard Deviation
Central	216 (6)	3035 (52)	195 (11)	208 (28)	0 (0)	3654	730.8	1291.20
Mid periphery	3183 (84)	1377 (24)	50 (3)	429 (57)	56 (49)	5095	1019	1325.28
Far periphery	409 (10)	1389 (24)	1544 (86)	119 (15)	57 (51)	3518	703.6	711.12
Total	3808	5801	1789	756	113	12 667		

Data are presented as no. (%) unless otherwise indicated. Note eyes 1 and 2 showed clinical evidence of age-related macular degeneration.

in eyes with clinical indications of AMD were significantly larger than those that formed in normal aged human eyes.

It has been proposed that calcified spherules play a key role in drusen biogenesis, potentially through acting as binding sites for proteins and lipids in the sub-RPE—BL space.[13] High-resolution electron micrographs are presented that support the mechanism for drusen biogenesis and growth proposed by Thompson et al.[13] Using high-resolution SEM, individual spherules without extracellular material were observed between the basal lamina of the RPE and the inner collagenous layer of BrM (Fig 2). These micrographs were highly comparable with the second stage (accumulation of hydroxyapatite-encrusted lipid particles) of drusen biogenesis and growth proposed by Thompson et al.[13] After further examination of the RPE—choroid complex in aged human eyes, small focal drusen that comprised individual or pairs of spherules surrounded by homogenous extracellular material also were observed. These were remarkably similar in morphologic features to the drusen described in the final stage of the mechanism by Thompson et al.[13] Importantly, the present study identified multiple large drusen that contained tens to hundreds of micrometer-sized spherules (Fig 1C—F), potentially reflecting an additional stage that was not proposed previously. Therefore, this study provides high-resolution microscopic evidence for the mechanism of deposit biogenesis proposed by Thompson et al, but also expands this model by identifying an additional stage that possibly reflects a later phase of AMD pathogenesis.

Alongside our high-resolution imaging approach, previous studies also provided evidence supporting the role of hydroxyapatite spherules in sub-RPE—BL deposit formation.[13,22] A study that combined immunohistochemical labelling of known drusen proteins with the use of a hydroxyapatite-specific fluorescent dye demonstrated the localization of proteins to the surface of hydroxyapatite spherules.[13] More recently, a proteomic study that analyzed plasma samples from patients with late-stage AMD identified elevated levels of hydroxyapatite binding proteins in plasma. Therefore, it is possible that proteins of choroidal origin are contributing to sub-RPE—BL deposit enlargement via binding to the surface of hydroxyapatite spherules in the sub-RPE—BL space.[22]

In the present investigation, spherical particles were observed that ranged from 0.12 to 12.53 μm in diameter with a mean and median of 1.74 μm and 1.55 μm, respectively. In-depth analysis revealed that the interquartile range of all examined spherules was 1.08 to 2.17 μm, consistent with the diameter of spherules reported in other diseases characterized by ectopic calcification, such as atherosclerosis.[13,17,23–26] Factors capable of influencing the size of calcified spherules remain unknown; however, spherule size may be determined by the molecules that nucleate its mineral precipitation. Therefore, potential candidates would have to be smaller in diameter than the spherule. Using a lipid-preserving methodology, lipid particles that were 80 to 100 nm in diameter were identified within hard drusen, the sub-RPE—BL space, and lesions occurring before the formation of basal linear deposits.[6,27,28] These particles were shown to contain both esterified and unesterified cholesterol.[27] Consistent with this, a recent study that used time-of-flight secondary ion mass spectrometry provided direct evidence that spherical particles possessed a cholesterol core that was encrusted within a hydroxyapatite shell.[13] Thus, it is possible that cholesterol droplets located within the sub-RPE—BL space or within lesions occurring before the formation of basal linear deposits could nucleate the precipitation of hydroxyapatite spherules that subsequently mediate sub-RPE—BL deposit formation and growth.

Spherical particles that accumulate within the sub-RPE—BL space of eyes with clinical indications of AMD exhibited a significantly larger diameter compared with those that accumulate within the sub-RPE—BL space of normal aged eyes. Importantly, a marked increase in the frequency of these larger particles was observed in eyes with AMD compared with those without. Although statistical confirmation of this latter finding will require a larger sample size, the increased frequency of larger spherules in eyes with clinical indications of AMD suggests that these particles likely are associated with this blinding disorder. Recently, it was shown that sub-RPE—BL deposits containing large (> 20 μm) multilobed nodules formed of hydroxyapatite were associated independently and significantly with progression to advanced stages of AMD (odds ratio, 6.36; $P < 0.001$).[19] Importantly, like many of the internal structures observed for spherical particles, the lobes of nodules also were composed of a distinct core and shell. Therefore, it is possible that the larger spherules observed in this study reflect an intermediate stage that occurs before the formation of these multilobed nodules, possibly indicating a change to the sub-RPE—BL microenvironment. It was hypothesized previously that increased extracellular calcium concentration, reduced magnesium concentration,

and a neutral pH in the sub-RPE−BL space may drive the preferential precipitation of nodules over spherules.[19] Thus, the larger spherules observed in eyes with clinical indications of AMD may suggest a change in the microenvironment that is optimal for disease onset, progression, or both.

The distribution of spherical particles across the central−far peripheral axis in aged human eyes (n = 5) also was investigated. Statistical analysis found no significant differences in the frequency of spherules in the central region, mid periphery, or far periphery of aged human eyes. This can be explained, in part, by the variation observed between individuals and the limited numbers of eyes available in this study (Table 3). Thus, our data suggest that the precipitation of spherical particles is ubiquitous across the human eye, possibly reflecting a systemic issue that results in changes to the microenvironment in the sub-RPE−BL space.

Differences in surface topography and internal structure between spherules also was observed in this study. How this heterogeneity occurs remains unknown. One possible explanation is that the internal structure, surface topography, or both are related to the mineral phase from which individual spherules have formed. A recent study reported that some spherical particles could be formed of whitlockite, a magnesium substituted tricalcium phosphate; however, the accumulation of other calcium phosphate minerals cannot be excluded.[13,19] Evidence supporting this hypothesis includes the distinct crystal structures of hydroxyapatite and whitlockite: hydroxyapatite crystals display hexagonal morphologic features (space group, P6$_3$/m), whereas whitlockite crystals exhibit rhombohedral structure (space group, R3c).[29] In addition, the substitution of Mg^{2+} ions into the developing whitlockite crystal results in a reduction in crystallite size compared with hydroxyapatite, potentially impacting spherule morphologic features.[24,25] Thus, it is plausible that the topography, internal structure, or both of spherules is related directly to the mineral phase from which they have formed.

Despite the large number of spherules analyzed in this study, limitations remained. For example, the small sample size used in this investigation prevented statistical analysis of the total number of spherules present in cross-sections of eyes with and without clinical evidence of AMD. Thus, to confirm this, a larger cohort of eyes would need to be analyzed. Moreover, improved tissue preservation would enable better detection of anatomic features (e.g., fovea, optic nerve head), allowing for precise identification of the central, mid-peripheral, and far-peripheral regions. Accordingly, this would facilitate better translation to clinical imaging methods. Furthermore, improved tissue preservation may enable the evaluation of RPE health and morphologic features above sub-RPE−BL deposits, spherules, or both, possibly providing greater insights into the role of spherules during AMD pathogenesis. Finally, owing to the hard material of spherules, internal structures were visible only on rare occasions when spherules cracked open as a result of diamond knife ultramicrotomy. Accordingly, a full quantitative assessment of internal structures could not be performed.

The data presented in this study suggests that the precipitation of calcific spherical particles in the sub-RPE−BL space is ubiquitous across the central−peripheral axis and that precipitation occurs in both healthy aged eyes as well as in eyes with clinical indications of AMD. However, appreciable differences in size, surface topography, and internal structure are present that potentially reflect differences in the localized microenvironment in which sub-RPE−BL deposits are formed. Larger and more numerous hydroxyapatite spherules are likely to lead to marked disruption of the RPE−choroid interface compared with smaller spherical particles. Therefore, understanding how changes in the local microenvironment facilitate hydroxyapatite spherule formation and growth and the subsequent biogenesis and enlargement of sub-RPE−BL deposits may help to develop treatment strategies that prevent or slow disruption of the RPE−choroid interface.

Acknowledgments

Footnotes and Disclosures

[1] University College London Institute of Ophthalmology, London, United Kingdom.

[2] Division of Biomaterials and Tissue Engineering, University College London Eastman Dental Institute, Royal Free Hospital, London, United Kingdom.

[3] Centre for Experimental Medicine, School of Medicine, Dentistry and Biomedical Science, Queen's University Belfast, Belfast, United Kingdom.

[4] Barts and The London School of Medicine and Dentistry, London, United Kingdom.

[5] Department of Materials, Imperial College London, London, United Kingdom.

[6] Roche Pharma Research and Early Development, Immunology, Infectious Diseases and Ophthalmology (I20) Discovery and Translational Area, Roche Innovation Centre Basel, F. Hoffmann-La Roche, Ltd., Basel, Switzerland.

[7] Department of Ophthalmology, Albert Eye Research Institute, and Department of Pathology, Duke University School of Medicine, Durham, North Carolina.

[8] Department of Biochemistry and Molecular Biology, University of Maryland School of Medicine, Baltimore, Maryland.

References

1. Sarks SH. Council lecture. Drusen and their relationship to senile macular degeneration. *Aust J Ophthalmol*. 1980;8(2):117−130.
2. Csincsik L, MacGillivray TJ, Flynn E, et al. Peripheral retinal imaging biomarkers for Alzheimer's disease: a pilot study. *Ophthalmic Res*. 2018;59(4):182−192.
3. Bergen AA, Arya S, Koster C, et al. On the origin of proteins in human drusen: the meet, greet and stick hypothesis. *Prog Retin Eye Res*. 2019;70:55−84.
4. Hageman GS, Luthert PJ, Victor Chong NH, et al. An integrated hypothesis that considers drusen as biomarkers of immune-mediated processes at the RPE-Bruch's membrane interface in aging and age-related macular degeneration. *Prog Retin Eye Res*. 2001;20(6):705−732.
5. Duvall-Young J, MacDonald MK, McKechnie NM. Fundus changes in (type II) mesangiocapillary glomerulonephritis simulating drusen: a histopathological report. *Br J Ophthalmol*. 1989;73(4):297−302.
6. Chen L, Messinger JD, Kar D, et al. Biometrics, impact, and significance of basal linear deposit and subretinal drusenoid deposit in age-related macular degeneration. *Invest Ophthalmol Vis Sci*. 2021;62(1):33.
7. Sura AA, Chen L, Messinger JD, et al. Measuring the contributions of basal laminar deposit and Bruch's membrane in age-related macular degeneration. *Invest Ophthalmol Vis Sci*. 2020;61(13):19.
8. Klein R, Klein BEK, Linton KLP. Prevalence of age-related maculopathy: The Beaver Dam Eye Study. *Ophthalmology*. 1992;99(6):933−943.
9. Khan KN, Mahroo OA, Khan RS, et al. Differentiating drusen: drusen and drusen-like appearances associated with ageing, age-related macular degeneration, inherited eye disease and other pathological processes. *Prog Retin Eye Res*. 2016;53:70−106.
10. Ukalovic K, Cao S, Lee S, et al. Drusen in the peripheral retina of the Alzheimer's eye. *Curr Alzheimer Res*. 2018;15(8):743−750.
11. Pauleikhoff D, Barondes MJ, Minassian D, et al. Drusen as risk factors in age-related macular disease. *Am J Ophthalmol*. 1990;109(1):38−43.
12. Pauleikhoff D, Harper CA, Marshall J, Bird AC. Aging changes in Bruch's membrane. A histochemical and morphologic study. *Ophthalmology*. 1990;97(2):171−178.
13. Thompson RB, Reffatto V, Bundy JG, et al. Identification of hydroxyapatite spherules provides new insight into subretinal pigment epithelial deposit formation in the aging eye. *Proc Natl Acad Sci U S A*. 2015;112(5):1565−1570.
14. Klien BA. The heredodegeneration of the macula lutea*: diagnostic and differential diagnostic considerations and a histopathologic report. *Am J Ophthalmol*. 1950;33(3 Part 1):371−379.
15. Donald J, Gass M. Pathogenesis of disciform detachment of the neuroepithelium: III. Senile disciform macular degeneration. *Am J Ophthalmol*. 1967;63(3 Part 2):617−645, 644/672.
16. Green WR, Key 3rd SN. Senile macular degeneration: a histopathologic study. *Trans Am Ophthalmol Soc*. 1977;75:180−254.
17. Ulshafer RJ, Allen CB, Nicolaissen JB, Rubin ML. Scanning electron microscopy of human drusen. *Invest Ophthalmol Vis Sci*. 1987;28(4):683−689.
18. Flinn JM, Kakalec P, Tappero R, et al. Correlations in distribution and concentration of calcium, copper and iron with zinc in isolated extracellular deposits associated with age-related macular degeneration. *Metallomics*. 2014;6(7):1223−1228.
19. Tan ACS, Pilgrim MG, Fearn S, et al. Calcified nodules in retinal drusen are associated with disease progression in age-related macular degeneration. *Sci Transl Med*. 2018;10(466):eaat4544.
20. Tan PL, Bowes Rickman C, Katsanis N. AMD and the alternative complement pathway: genetics and functional implications. *Hum Genomics*. 2016;10(1):23.

21. Domalpally A, Clemons TE, Danis RP, et al. Peripheral retinal changes associated with age-related macular degeneration in the Age-Related Eye Disease Study 2: Age-Related Eye Disease Study 2 report number 12 by the Age-Related Eye Disease Study 2 Optos PEripheral RetinA (OPERA) Study Research Group*. *Ophthalmology*. 2017;124(4):479−487.

22. Arya S, Emri E, Synowsky SA, et al. Quantitative analysis of hydroxyapatite-binding plasma proteins in genotyped individuals with late-stage age-related macular degeneration. *Exp Eye Res*. 2018;172:21−29.

23. Tsolaki E, Bertazzo S. Pathological mineralization: the potential of mineralomics. *Materials (Basel)*. 2019;12(19):3126.

24. Schlieper G, Aretz A, Verberckmoes SC, et al. Ultrastructural analysis of vascular calcifications in uremia. *J Am Soc Nephrol*. 2010;21(4):689−696.

25. Shah FA, Lee BEJ, Tedesco J, et al. Micrometer-sized magnesium whitlockite crystals in micropetrosis of bisphosphonate-exposed human alveolar bone. *Nano Lett*. 2017;17(10):6210−6216.

26. Bertazzo S, Gentleman E, Cloyd KL, et al. Nano-analytical electron microscopy reveals fundamental insights into human cardiovascular tissue calcification. *Nat Mat*. 2013;12(6):576−583.

27. Curcio CA, Millican CL, Bailey T, Kruth HS. Accumulation of cholesterol with age in human Bruch's membrane. *Invest Ophthalmol Vis Sci*. 2001;42(1):265−274.

28. Ruberti JW, Curcio CA, Millican CL, et al. Quick-freeze/deep-etch visualization of age-related lipid accumulation in Bruch's membrane. *Invest Ophthalmol Vis Sci*. 2003;44(4):1753−1759.

29. Cheng H, Chabok R, Guan X, et al. Synergistic interplay between the two major bone minerals, hydroxyapatite and whitlockite nanoparticles, for osteogenic differentiation of mesenchymal stem cells. *Acta Biomater*. 2018;69:342−351.